ACS OMEGA

http://pubs.acs.org/journal/acsodf

Article

# Functionalized Sulfide Solid Electrolyte with Air-Stable and Chemical-Resistant Oxysulfide Nanolayer for All-Solid-State Batteries

Wo Dum Jung,[#] Minjae Jeon,[#] Sung Soo Shin, Ji-Su Kim, Hun-Gi Jung, Byung-Kook Kim, Jong-Heun Lee, Yong-Chae Chung,* and Hyoungchul Kim*

Cite This: *ACS Omega* 2020, 5, 26015−26022

Read Online

ACCESS | Metrics & More | Article Recommendations | Supporting Information

**ABSTRACT:** Sulfide solid electrolytes (SEs) with high Li-ion conductivities ($\sigma_{ion}$) and soft mechanical properties have limited applications in wet casting processes for commercial all-solid-state batteries (ASSBs) because of their inherent atmospheric and chemical instabilities. In this study, we fabricated sulfide SEs with a novel core−shell structure via environmental mechanical alloying, while providing sufficient control of the partial pressure of oxygen. This powder possesses notable atmospheric stability and chemical resistance because it is covered with a stable oxysulfide nanolayer that prevents deterioration of the bulk region. The core−shell SEs showed a $\sigma_{ion}$ of more than 2.50 mS cm$^{-1}$ after air exposure (for 30 min) and reaction with slurry chemicals (mixing and drying for 31 min), which was approximately 82.8% of the initial $\sigma_{ion}$. The ASSB cell fabricated through wet casting provided an initial discharge capacity of 125.6 mAh g$^{-1}$. The core−shell SEs thus exhibited improved powder stability and reliability in the presence of chemicals used in various wet casting processes for commercial ASSBs.

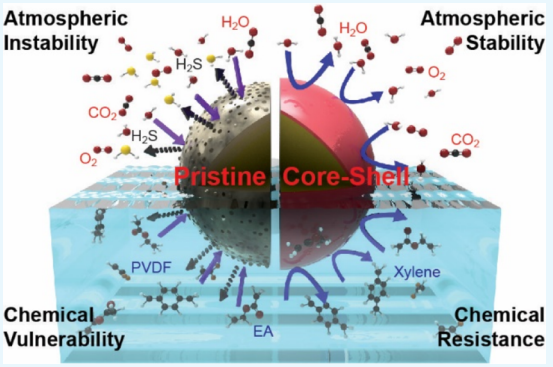


## INTRODUCTION

In recent years, all-solid-state batteries (ASSBs) have become widely recognized as promising next-generation batteries because of their high energy densities, wide range of operating conditions, and high safety.[1−5] Various solid electrolytes (SEs) employed in ASSBs have been reported to be important components for stable cell fabrication and operation.[5−8] In particular, sulfides are one of the most effective SE materials because they have superior Li-ion conductivity ($\sigma_{ion}$) compared to other SEs. Moreover, they exhibit ductile mechanical properties that are advantageous for formation at room temperature.[8−10] Recently, several sulfide SEs have been discovered with a $\sigma_{ion}$ of more than 10 mS cm$^{-1}$, which is comparable to that of the liquid electrolytes used in conventional Li-ion batteries.[5,8,11,13] However, the atmospheric and chemical stabilities of sulfides have not been examined in detail. Generally, the high $\sigma_{ion}$ of sulfide SEs deteriorates on account of the moisture and oxygen contents in the atmosphere.[14−21] Therefore, these SEs must be utilized in specific equipment or spaces where moisture and oxygen are extremely low.[2,5,7,9,12] These difficulties must be overcome because they increase the cost of material synthesis and decrease the reliability of the ASSB material properties in commercialization.

Numerous researchers have used the most common and efficient methods for improving the atmospheric instability and chemical vulnerability of sulfides. Specifically, they have employed solid solution (or composite) processes with oxides that comprise the same crystal structure and exhibit much greater stability,[18−22] *i.e.*, $Li_2S-P_2S_5$ partially substituted (or mixed) with $P_2O_5$ (or metal oxides).[18,20,21] However, as the amount of oxide increases, the $\sigma_{ion}$ of the solid solution (or composite) significantly decreases from $10^{-2}$ to $10^{-1}$ mS cm$^{-1}$.[20,21] Furthermore, previous studies on improving the atmospheric stability of sulfides with oxides (or oxysulfides) were generally identified to incorporate oxides as the respective starting materials in powder synthesis.[18−22] This method changes the bulk characteristics of sulfides by compositing oxides and sulfides or by realizing a single oxysulfide phase in all areas of the material. The above studies successfully improved the atmospheric stability of sulfides by decreasing the amount of $H_2S$ gas generation; nevertheless, most of these studies could not prevent a significant decrease in $\sigma_{ion}$ or an increase in elastic moduli owing to their inevitable oxide

Received: July 19, 2020
Accepted: September 17, 2020
Published: October 1, 2020

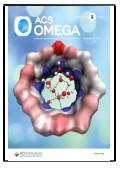






https://dx.doi.org/10.1021/acsomega.0c03453
*ACS Omega* 2020, 5, 26015−26022

characteristics. As a completely different approach, recent research has revealed the superior atmospheric stability of sulfides by replacing a hard acid (here, P) with soft acids (Sn and As).[15−17] According to the concept of using hard and soft acids and bases, the atmospheric stability can be improved by changing the reaction preference and replacing the reactive hard acid with soft acid cations. However, in that research, the issue of the toxicities of new elements emerged, and the stability of solvent/binder reactions beyond atmospheric stability was not assessed.[15,17]

In the present study, we synthesized a novel core−shell sulfide, *i.e.*, oxysulfide-coated $Li_6PS_5Cl$ argyrodite (hereafter denoted as OScA), by applying environmental mechanical alloying and controlling the oxygen partial pressure. We determined that the OScA powder maintained excellent Li-ion transport properties through improved atmospheric stability and chemical resistance compared with pristine argyrodite ($Li_6PS_5Cl$, hereafter referred to as PriA). Finally, by fabricating ASSBs and characterizing their performance, we determined the effectiveness of this novel oxysulfide nanolayer-coated sulfide and its potential as an SE material.

## RESULTS AND DISCUSSION

To fabricate the proposed sulfide SE coated with an oxysulfide nanolayer, we introduced environmental mechanical alloying, a new modification to the process of high-energy ball milling in an inert atmosphere. We divided this process into three planetary milling stages: (1) mixing the raw materials, (2) alloying in an inert atmosphere, and (3) coating in an oxidizing atmosphere. A detailed schematic of the environmental mechanical alloying is shown in Figure 1a. In the first stage, the $Li_2S$, $P_2S_5$ and LiCl raw starting materials were mixed in the molar ratio of 5:1:2. In the second stage, the mixture was converted into glass−ceramic argyrodites by introducing high-energy milling at an extremely low oxygen partial pressure for 8 h. In the third stage, the low oxygen partial pressure (Ar filled, $O_2 \leq 0.1$ ppm) was substituted by a high oxygen partial pressure ($O_2 \approx 1.493$ atm). This process deposited an extremely thin oxide coating layer on the glass−ceramic powders, thereby forming a core−shell structure that divides the oxide and sulfide regions into their respective core and shell structures. The shell structure was expected to have a high chemical stability to prevent structural degradation of the core sulfides and to increase the reliability of the powder during wet casting processes and cell operations.

We investigated the crystal structure and $\sigma_{ion}$ of the PriA and OScA samples for reference. The detailed X-ray diffraction (XRD) patterns are shown in Figure 1b. Both samples after high-temperature annealing at 500 °C clearly exhibit the $Li_6PS_5Cl$ argyrodite crystal phase with or without the oxysulfide shell structure. The average $\sigma_{ion}$ of OScA is 3.02 mS cm$^{-1}$ (standard deviation = 0.220) owing to the presence of the surface oxysulfide nanolayer. This $\sigma_{ion}$ is 10.4% lower than the average $\sigma_{ion}$ of PriA (3.37 mS cm$^{-1}$; standard deviation = 0.141). The activation energy of OScA corresponds to 0.33 eV from the Arrhenius equation of $\sigma_{ion}$. This value generally agrees with the results of pristine $Li_6PS_5Cl$, our PriA sample, and results in the literature (see Figure S1).[23−25] Additionally, we conducted cyclic voltammetry (CV) tests to investigate the difference in electrochemical stability window between PriA and OScA (see Figure S2). They identically show the well-known reduction and oxidation peaks at 1.8 and 2.6 V, respectively. These peaks are positioned

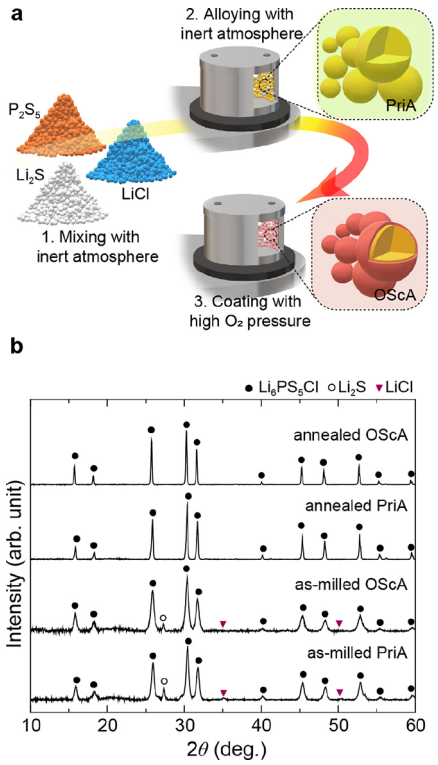


**Figure 1.** (a) Schematic of the environmental mechanical alloying process flow for preparing PriA and OScA powders. (b) XRD patterns of PriA and OScA powders before and after annealing. Reference XRD patterns of $Li_6PS_5Cl$ (PDF #04-018-1429), $Li_2S$ (PDF #98-064-2291), and LiCl (PDF #98-002-6909) are also marked.

at almost the same voltages as those of pristine $Li_6PS_5Cl$, as reported in the literature.[13,26,27]

We utilized transmission electron microcopy (TEM), energy dispersive X-ray spectroscopy (EDX), and X-ray photoelectron spectroscopy (XPS) to verify the existence of the oxysulfide nanolayer on the $Li_6PS_5Cl$ core structure. Figure 2 shows the

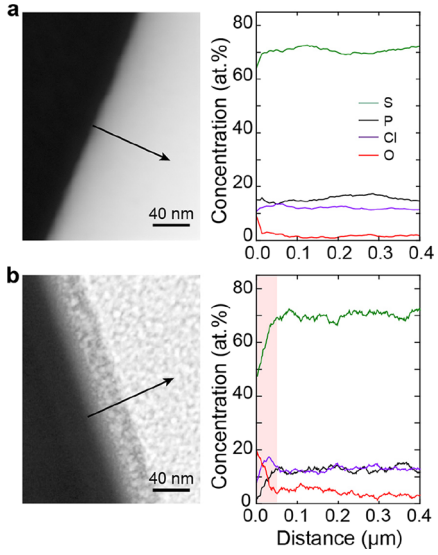


**Figure 2.** Surface structure characterization of (a) PriA and (b) OScA powders. Compositional line profiles of elements (S, P, Cl, and O) from each sample recorded along the arrow shown in each TEM image.



https://dx.doi.org/10.1021/acsomega.0c03453
ACS Omega 2020, 5, 26015−26022

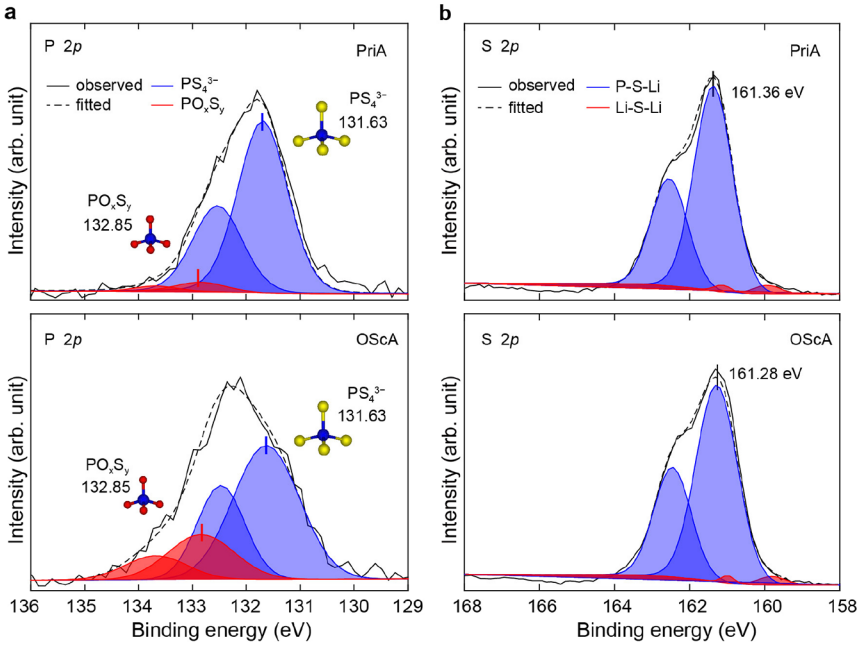


**Figure 3.** (a) P 2*p* XPS spectra for PriA and OScA samples. The blue region corresponds to the peak of the $PS_4^{3-}$ anion cluster; the red region is the $PO_xS_y$ peak. (b) S 2*p* XPS spectra for PriA and OScA samples. The red and blue regions correspond to the peaks of Li−S−Li and P−S−Li bonds, respectively.

surface microstructure of the PriA and OScA samples obtained from the TEM analysis and their element concentration profiles along the scanned line (from surface to bulk). The presence of this oxysulfide region was clearly observed in the TEM image of the OScA sample, with a unique 50 nm-thick nanolayer formed on the OScA surface. Further, the element profiles of both samples in the TEM-EDX analysis show different oxygen concentrations in their surface regions. The OScA sample contains an oxysulfide layer with approximately 15 at.% sulfur to oxygen substitution, while the PriA sample maintains a constant composition ratio across the surface and bulk regions.

Figure 3 presents further evidence by identifying the oxysulfide nanolayer using XPS analysis, which is a surface-sensitive quantitative spectroscopic technique. In the PriA and OScA samples, the P 2*p* peak corresponding to the binding energy of $PS_4^{3-}$ is predominantly identified (at 131.63 eV). The OScA sample shows another noticeable peak at 132.85 eV along with the common $PS_4^{3-}$ peak. This new peak at 132.85 eV is confirmed by the $PO_xS_y$ binding energy related to P, O, and S, which is consistent with the oxysulfide binding energy reported in the literature.[28−31] As shown in Figure 3b, the S 2*p* peak of the OScA sample appears at 161.28 eV, which is downshifted from the S-state of typical sulfides, suggesting the formation of oxysulfides in our OScA sample. In addition, the absence of sulfate species at about 168 eV also shows that both S and O atoms are chemically bound to cations. We also measured the Raman spectra to verify the presence of an oxysulfide nanolayer, as shown in Figure S3. The wavenumber of the OScA sample shifted to become higher than that of PriA. This high Raman shift indicates that sulfur in $PS_4^{3-}$ was replaced with a lighter element (here, oxygen).[32] Consequently, by comprehensively observing the microstructure and composition, and by analyzing the surface species, we confirmed the successful formation of ultrathin oxysulfide layers on the $Li_6PS_5Cl$ SEs. The formation was achieved by controlling the oxygen partial pressure during our proposed three-stage environmental milling process.

Because stability under real-world fabrication and operation conditions is a key requirement of sulfide-based ASSB materials, we characterized the atmospheric and chemical stability of our pristine and oxysulfide-coated SE materials by multiple methods. First, we assessed the atmospheric stability of the PriA and OScA samples under relative humidity (RH) 35% condition at 25 °C. The degradation behavior of the material observed with air exposure was investigated in terms of the XPS-based surface analysis and changes in $\sigma_{ion}$. The results of the XPS analysis are shown in Figure 4a. Before and after air exposure, the intensity of the O 1*s* peaks changed significantly, whereas the C 1*s* binding energy peaks of the two materials remained constant. As the OScA sample consists of an inherent oxysulfide nanolayer, the O 1*s* peak did not change after air exposure. However, the surface of the PriA sample oxidized because the surface was exposed to moisture and oxygen during air exposure. As a result, the O 1*s* peak rapidly increased. Therefore, the surface oxysulfide nanolayer of OScA prevented the atmosphere from degrading the surface of the sulfides. The detection of a small residual oxygen peak could not be avoided, even in an ultrahigh vacuum state, on account of the inherent features of XPS, which precisely measured the top surface of the sample.

Furthermore, the surface structure of the PriA sample without a surface layer rapidly degraded after atmospheric exposure. This deterioration was verified in terms of the changes in $\sigma_{ion}$ before and after air exposure under RH 35% at 25 °C. The results are shown in Figure 4b. Both samples exhibit the similar monotonic decrease in $\sigma_{ion}$ over 120 min. However, the changes in $\sigma_{ion}$ observed within 15 min and the degradation rate of air exposure are noteworthy (the degradation rates of PriA and OScA samples are −58.0 and −21.4 $\mu$S cm$^{-1}$ min$^{-1}$, respectively), as shown in an inset of Figure 4b. Specifically, the $\sigma_{ion}$ of PriA rapidly decreased by


https://dx.doi.org/10.1021/acsomega.0c03453
ACS Omega 2020, 5, 26015−26022

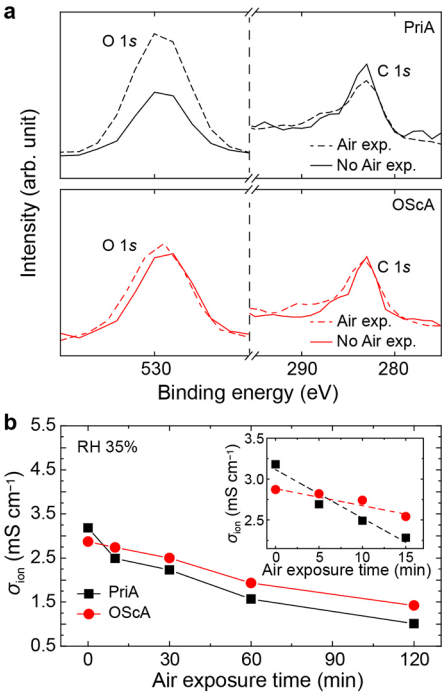


**Figure 4.** Atmospheric stability tests of PriA and OScA powders. (a) O 1*s* and C 1*s* XPS spectra of the PriA and OScA samples. Samples were tested before (solid lines) and after (dashed lines) air exposure for 30 min under RH 35% at 25 °C. (b) Variations in $\sigma_{ion}$ with RH 35% condition at 25 °C and air exposure time up to 120 min.

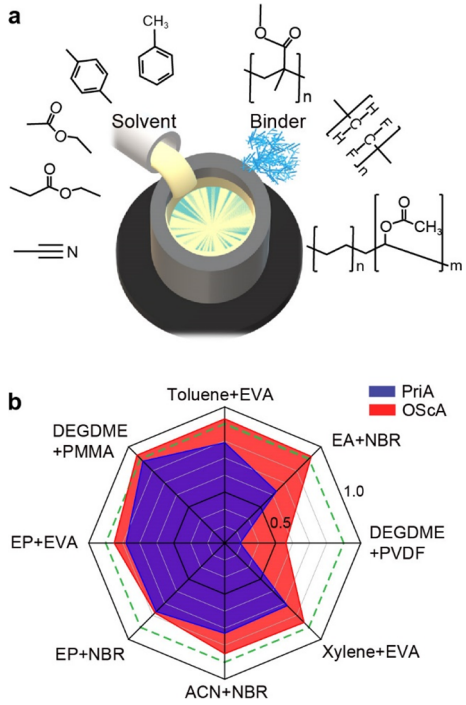


**Figure 5.** Chemical resistance tests of PriA and OScA powders. (a) Schematic illustration of chemical resistance tests with various solvents and binders. (b) Comparison of the $\sigma_{ion}$ ratio after chemical resistance tests. The $\sigma_{ion}$ ratio is the $\sigma_{ion}$ obtained after the chemical reactions divided by $\sigma_{ion,0}$, where $\sigma_{ion,0}$ is the initial $\sigma_{ion}$. The green dashed line indicates that the $\sigma_{ion}$ ratio is greater than 0.9.

approximately 21.7%, whereas the $\sigma_{ion}$ of OScA remained almost unchanged (less than 4.53% decrease). These results indicate that the thin oxysulfide nanolayer formed on the OScA powder suppressed the rapid deterioration of the sulfide SEs. These sulfide SEs exhibited uniform performance for a certain period of time after the initial exposure to the atmosphere. We confirmed the presence of a thick oxysulfide layer formed by providing more oxygen through control of the coating mill speed, as shown in Figure S4. Although it was possible to coat thicker and higher oxygen contents layers at coating mill speeds of 500 and 700 rpm, the decrease in the initial $\sigma_{ion}$ of the OScA sample was inevitable. The initial $\sigma_{ion}$ decreases as oxygen forms a thick film and oxygen penetrates deep into the bulk. Such OScA samples with thick oxysulfide layer have a low deterioration rate under the condition of RH 35%, but their actual $\sigma_{ion}$ is lower than that of PriA, limiting their practical merits. The relevant impedance spectra and detailed $\sigma_{ion}$ results of PriA and OScA as a function of the air exposure time at RH 35% condition are provided in Figure S5 and Table S1. Considering these time-dependent results obtained from harsh RH 35% condition at 25 °C, we conclude that the new OScA powder can maintain uniform material performance for conditions required to complete cell production.

In addition to the results on atmospheric stability, we verified the chemical resistance of the new material during the wet casting process. As shown in Figure 5a, the chemical resistance was characterized by reacting the PriA and OScA samples with solutions that were developed by combining various solvents and organic binders and then measuring $\sigma_{ion}$. First, the solubilities of the individual combinations of solvents and binders, which have been widely used in the slurry casting process for ASSBs, were examined.[33−37] Subsequently, only the combinations that completely dissolved the samples were selected, *i.e.*, toluene with ethylene-vinyl acetate (EVA), xylene with EVA, acetonitrile (ACN) with nitrile-butadiene rubber (NBR), ethyl propionate (EP) with EVA/NBR, ethyl acetate (EA) with NBR, and diethylene glycol dimethyl ether (DEGDME) with polymethyl methacrylate (PMMA)/polyvinylidene fluoride (PVDF). After the reaction with various solvent−binder solutions (room temperature vortex mixing for 1 min and high-temperature drying for 30 min), the $\sigma_{ion}$ of the two electrolytes were measured, and the ratios between the measured and initial values were obtained, as shown in Figure 5b. OScA exhibits generally better stability than PriA in nonpolar and polar solvent solutions. In particular, OScA showed a considerably smaller decrease in $\sigma_{ion}$ than PriA in ACN-based and EA-based solutions, which are more polar than xylene (polar indices of ACN, EA, and xylene are 5.8, 4.4, and 2.5, respectively).[38,39] Unlike typical sulfide SEs that show structural degradation owing to the nucleophilic attack of highly polar solvents,[36,40−42] the OScA material exhibited some resistance to both solvents and binders. This is because the oxysulfide nanolayer formed on the powder surface effectively suppressed the direct chemical reaction between the sulfides and organics, including the solvent and binder.

Among the results shown in Figure 5b, the results obtained using the combination of the EA solvent and NBR binder were quite interesting. In accordance with the typical properties of the sulfides that are vulnerable to highly polar solvents, the observed decrease in $\sigma_{ion}$ was ∼37% in the PriA sample and less than 8% in the OScA sample, which exhibited a $\sigma_{ion}$ ratio of 0.9. An important point is that EA has higher polarity than EP; however, the low boiling point (BP) of EA is advantageous for drying,[43] which can reduce the amount of the residual


https://dx.doi.org/10.1021/acsomega.0c03453
ACS Omega 2020, 5, 26015−26022

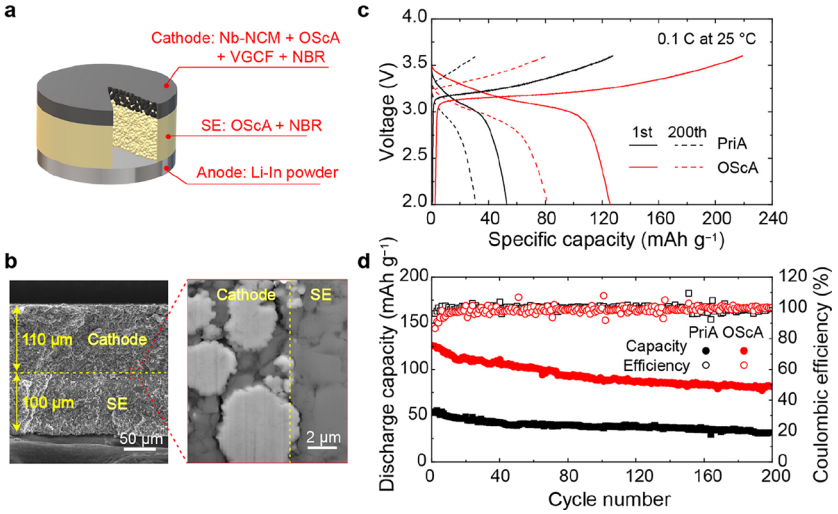


**Figure 6.** (a) Schematic illustration and (b) cross-sectional SEM image of an ASSB (cathode/SE/Li−In) cell used for electrochemical performance tests. (c) Charge/discharge profiles of the 1 and 200 cycles at 0.1 C. (d) Discharge capacity and Coulombic efficiency during 200 cycles of PriA and OScA cells at 0.1 C.

organic content. Moreover, the results of using toluene and xylene need to be noted. Both solvents containing EVA binder showed similar notable differences in PriA and OScA. Toluene has slightly higher polarity than xylene; however, it has a low BP,[37] which is good for drying. Therefore, in choosing a solvent, it is necessary to consider the effects of both polarity and BP. Lastly, our experimental results showed that the binder polarity is also a very important consideration in wet casting. Because PVDF binders have C-F functional groups, they have higher polarity than other binders,[44] resulting in the very low $\sigma_{ion}$ of the PriA and OScA materials. In contrast, NBR, which has lower polarity than PVDF, shows a small decrease in $\sigma_{ion}$.[44] As a result, we confirmed that the OScA material has higher usability for polar solvents (*e.g.*, EA and toluene) than the nonpolar solvents (*e.g.*, xylene) commonly used for wet casting process. Thus, this material is suitable for a process with more favorable conditions for wet casting (use of various binders, control of the binder content with high solubility, and improvement of casting quality using highly adhesive binders).[36,37,45]

To characterize the cell performance, as described in the following section, we selected and applied a combination of EA solvents and NBR binders. EA, which is typically not used as a solvent because of its relatively high polarity, has a low boiling point (77 °C) and a high vapor pressure (~9.73 kPa at 20 °C). These characteristics provide the advantage of easy and rapid slurry drying.[46] The OScA material developed in this study showed extremely high chemical resistance in EA solvents combined with the NBR binders. Consequently, cell fabrication and characterization were possible with these components.

Figure 6 shows the microstructure and cell performance of an ASSB cell prepared using the OScA material as an SE. As described in the experimental section and Figure 6a, the ASSB cell was prepared by wet casting the electrolyte (PriA or OScA) and composite cathode [$LiNbO_3$ coated $LiNi_{0.6}Co_{0.2}Mn_{0.2}O_2$ (Nb-NCM), SE, and vapor-grown carbon fiber (VGCF)] in the form of a tape sheet and bonding them by employing a uniaxial lamination process. As shown in scanning electron microscope (SEM) images of Figure 6b, we confirmed that the ASSB cell microstructure was well prepared with no noticeable interface cracks and macropores in the laminated tape sheets. Figure 6c,d shows the initial charge/discharge capacity and cycle performance over 200 cycles of the ASSB cells prepared using OScA and PriA. The initial discharge capacity of the ASSB cell with OScA was 125.6 mAh $g^{-1}$ (areal initial discharge capacity of 0.711 mAh $cm^{-2}$) and a discharge capacity of 81.36 mAh $g^{-1}$ was maintained even after 200 cycles. However, the ASSB cell with PriA showed a poor initial discharge capacity of 52.7 mAh $g^{-1}$, which decreased to less than 30.96 mAh $g^{-1}$ after 200 cycles. This notable difference in the performance of the cells with PriA and OScA can be attributed to the significant degradation of PriA during the wet casting process on account of the polar EA solvent. On the contrary, we confirmed that the oxysulfide nanolayer, which formed on the surface of the OScA powder, was observed to enhance the chemical resistance to the polar solvent and binder, which rendered OScA extremely suitable for the entire wet casting process.

## CONCLUSIONS

In summary, a novel core−shell SE material that exhibited notable atmospheric stability and chemical resistance was prepared via an environmental mechanical alloying technique, in which the oxygen partial pressure was controlled. The annealed OScA powder, a sulfide SE coated with a 50 nm-thick oxysulfide nanolayer as a protective layer, initially had an average $\sigma_{ion}$ of 3.02 mS $cm^{-1}$ at 25 °C. This core−shell SEs showed a $\sigma_{ion}$ of more than 2.50 mS $cm^{-1}$ after air exposure (30 min, RH 35% at 25 °C) and reaction with slurry chemicals (EA with NBR; room temperature vortex mixing for 1 min and high-temperature drying for 30 min), which was approximately 82.8% of the initial $\sigma_{ion}$. These results were interesting, considering that the $\sigma_{ion}$ of the PriA sample without the oxysulfide nanolayer was degraded by 35% or more.

Based on these results, we fabricated ASSB cells with OScA and PriA by employing a wet casting process using the polar solvent EA and NBR as a binder. We evaluated the charge and discharge performance. The initial discharge capacity of the cell with OScA was 125.6 mAh $g^{-1}$, which was approximately 138% higher than that of the cell with PriA. Furthermore, the cell with OScA was considerably more stable even after 200


https://dx.doi.org/10.1021/acsomega.0c03453
ACS Omega 2020, 5, 26015−26022

cycles. These results provide new possibilities for improving the atmospheric and chemical stabilities of sulfide SE materials, and they are expected to contribute to a major breakthrough in the commercialization of ASSBs.

## METHODS

**Powder Preparation.** The starting materials, *i.e.*, $Li_2S$ (Aldrich, 99.9%), $P_2S_5$ (Aldrich, 99%), and LiCl (Aldrich, 99%), were mixed according to a stoichiometry of 5:1:2. For preparing the PriA sample, the mixture was placed in a $ZrO_2$ bowl (P5 Premium Line, Fristch) along with 3 mm $ZrO_2$ beads. It was milled at 700 rpm for 9 h under extremely low partial pressure of oxygen (*i.e.*, argon atmosphere; $O_2 \leq 0.1$ ppm). In contrast, the OScA sample was milled at 700 rpm for 8 h under the same atmosphere ($O_2 \leq 0.1$ ppm), and then the obtained powder was additionally milled for 1 h at 300 rpm in a high partial pressure of oxygen ($O_2 \approx 1.493$ atm). A container lid with gas inlet pipes was used to apply the high pressure oxygen gas (purity 99.999%), and the container was sealed with a clamp to withstand high pressure. After the milling process, both samples were added to quartz tubes and heated to 500 °C for 2 h (ramp rate = 10 °C $min^{-1}$) in an argon atmosphere. Then, the quartz tubes were rapidly cooled to room temperature. The final products were ground into a fine powder using an agate mortar. The relevant schematic illustration showing the process flow of PriA and OScA powders is shown in Figure 1a.

**Powder Characterization.** The crystal structures of the as-milled and final samples were characterized by utilizing a powder X-ray diffractometer (D8 Advance, Bruker) with Cu K$\alpha$ radiation ($\lambda$ = 1.540598 Å). The samples were placed on a silicon zero background holder and covered with a Kapton polyimide film to prevent possible moisture and oxygen uptake. XRD patterns were collected over a 2$\theta$ range of 10−70° at intervals of 0.02°. The thickness of the coating layer for the OScA sample was determined from the line profiles obtained from TEM (Talos F200X, FEI; Titan TM 80-300, FEI) and EDX (Super-X EDS system, Bruker; PV97-61850-ME, EDAX) mapping. The sample was placed on a copper TEM grid coated with a carbon film. The TEM grid was placed in a double-tilt vacuum transfer holder (model 648, GATAN) to prevent exposure to the atmosphere. XPS (PHI 5000 VersaProbe, ULVAC PHI) was performed on the PriA and OScA samples to accurately identify the elemental composition of the surfaces of the samples. High-resolution scans were collected in the Li 1*s*, P 2*p*, O 1*s*, S 2*p*, C 1*s*, and Cl 2*p* energy regions with a monochromatic Al K$\alpha$ source (1486.6 eV) at a base pressure of $2 \times 10^{-7}$ Pa. The binding energy was calibrated with the C 1*s* peak (set to 284.6 eV). Raman spectra measurements of the PriA and OScA samples were conducted with a spectrometer (LabRam Aramis spectrometer, Horiba JobinYvon) using a wavelength of 514.5 nm. The Raman spectroscopy data were collected in the frequency range of 0 to 700 $cm^{-1}$, and each spectrum was measured at a resolution of 0.5 $cm^{-1}$ for 60 s. All Raman spectra were corrected with multiline baseline correction. For evaluating the Li metal stability of the PriA and OScA samples, CV measurements of asymmetric cell (Li/SE/SE-carbon/Pt) were performed from −0.04 to 5 V with a scan rate of 0.2 mV $s^{-1}$ at 25 °C. This rigorous CV setup, which was presented in recent papers,[13,26] improves the interface contact between the SE and electrode to effectively verify the electrochemical stability window. The $\sigma_{ion}$ results at 25 °C were measured using a frequency response analyzer (model 1260, Solartron) and electrochemical interface equipment (model 1287, Solartron). All samples were uniaxially cold-pressed under 300 MPa for analyzing $\sigma_{ion}$. The $\sigma_{ion}$ of a pellet was measured by applying a voltage of 100 mV in a frequency range of $10^2$ to $10^6$ Hz. Variations of $\sigma_{ion}$ with temperature (up to 120 °C) were measured by applying the same cold-pressed pellet and impedance setup.

Atmospheric stability tests were performed by using a constant temperature and humidity chamber (Rcom Max 50, Rcom). We established the chamber conditions (relative humidity, RH, of 35% at 25 °C), and 0.2 g of the as-annealed OScA and PriA powders in the vial bottle (4 mL volume) were exposed to the controlled atmosphere. The chemical stability of both samples was measured using various types of solvents and binders such as DEGDME, EA, *p*-xylene, toluene, ACN, EP, PMMA, PVDF, EVA, and NBR. The slurry was prepared by stirring and dissolving the electrolyte, solvent, and binder at a weight ratio of 50:49.3:0.7 for 1 min using a vortex mixer. All slurries except the DEGDME-based slurry (at 280 °C) were dried on a hot plate at 240 °C for 30 min. All samples synthesized and prepared in an inert gas atmosphere ($O_2 \leq 0.1$ ppm).

**Cell Fabrication and Characterization.** The composite cathode consisted of four components; the active material (Nb-NCM), the PriA or OScA SE, a conductive agent (VGCF), and a binder (NBR), at a weight ratio of 60:36:4:1.37. Each mixture was placed in a stainless steel bowl with stainless steel balls and EA and then dispersed for 9 min using a vibration mixing mill (MM400, Retsch). The slurry for the PriA or OScA SE layer was created using the SE powder, NBR, and EA and mixed using a vibration mixing mill under operation condition. The electrode and electrolyte were cast on an aluminum foil and a polyimide film, respectively. The two castings were created with a thickness of 200 $\mu$m via an auto caster and dried for 3 h at room temperature. The cast electrolyte layer (CEL) was fed into a 10 mm mold and compressed at 151 MPa. The cast composite cathode and CEL were placed into the same mold facing each other and pressed at 267 MPa. As the counter electrode, Li−In powder was added on the other side of the SE pellet, and the three layers were pressed at 98 MPa. The three-layered pellet was assembled into a CR2032-type coin cell for electrochemical characterization. The cell performance was tested in a voltage range of 2.0−3.6 V (vs Li) at 25 °C using a battery testing system (4300 K Desktop, Maccor). The current density at a C-rate of 1C was set as 180 mA $g^{-1}$, and the specific capacity was calculated based on the weight of NCM in the coin cell. The cells were charged in the constant−current/constant−voltage (CC-CV) mode and discharged in the CC mode. The interface between the composite cathode and the electrolyte layer of the cell was observed using a SEM (Quanta 3D, FEI) at 30 kV. The sample was prepared by tilting the cell at 52° using an ion beam from a $Ga^+$ source, and the surface of the sample was milled with a focused ion beam.

## ASSOCIATED CONTENT

### Supporting Information

The Supporting Information is available free of charge at https://pubs.acs.org/doi/10.1021/acsomega.0c03453.

Arrhenius plot of Li-ion conductivity in PriA and OScA samples, electrochemical and atmospheric stability tests of PriA and OScA samples, surface structure analysis of



https://dx.doi.org/10.1021/acsomega.0c03453
ACS Omega 2020, 5, 26015−26022

PriA and OScA samples, and detailed data sets of measured Li-ion conductivities of PriA and OScA samples after air exposure under RH 35% at 25 °C (PDF)

## AUTHOR INFORMATION


### Corresponding Authors

**Yong-Chae Chung** − *Department of Materials Science and Engineering, Hanyang University, Seoul 04763, Republic of Korea*; Email: yongchae@hanyang.ac.kr

**Hyoungchul Kim** − *Center for Energy Materials Research, Korea Institute of Science and Technology, Seoul 02792, Republic of Korea*; orcid.org/0000-0003-3109-660X; Email: hyoungchul@kist.re.kr

### Authors

**Wo Dum Jung** − *Center for Energy Materials Research, Korea Institute of Science and Technology, Seoul 02792, Republic of Korea; Department of Materials Science and Engineering, Korea University, Seoul 02841, Republic of Korea*

**Minjae Jeon** − *Center for Energy Materials Research, Korea Institute of Science and Technology, Seoul 02792, Republic of Korea; Department of Materials Science and Engineering, Hanyang University, Seoul 04763, Republic of Korea*

**Sung Soo Shin** − *Center for Energy Materials Research, Korea Institute of Science and Technology, Seoul 02792, Republic of Korea*

**Ji-Su Kim** − *Center for Energy Materials Research, Korea Institute of Science and Technology, Seoul 02792, Republic of Korea*

**Hun-Gi Jung** − *Center for Energy Storage Research, Korea Institute of Science and Technology, Seoul 02792, Republic of Korea*; orcid.org/0000-0002-2162-2680

**Byung-Kook Kim** − *Center for Energy Materials Research, Korea Institute of Science and Technology, Seoul 02792, Republic of Korea*

**Jong-Heun Lee** − *Department of Materials Science and Engineering, Korea University, Seoul 02841, Republic of Korea*; orcid.org/0000-0002-3075-3623

Complete contact information is available at: https://pubs.acs.org/10.1021/acsomega.0c03453


### Author Contributions

#W.D.J. and M.J. contributed equally to this work.

### Notes

The authors declare no competing financial interest.

## ACKNOWLEDGMENTS

This work was supported by the National Research Foundation of Korea (NRF) grant funded by the Korea Government (MSIT) (no. 2020R1A2C2010191). This research was also funded in part by the Institutional Research Program of the KIST (no. 2E30202). The work was partly supported by the Technology Development Program to Solve Climate Changes of the Korean National Research Foundation (NRF) (no. 2017M1A2A2044482).

## REFERENCES


(1) Inoue, T.; Mukai, K. Are All-Solid-State Lithium-Ion Batteries Really Safe?−Verification by Differential Scanning Calorimetry with an All-Inclusive Microcell. *ACS Appl. Mater. Interfaces* **2017**, *9*, 1507−1515.

(2) Kato, Y.; Kawamoto, K.; Kanno, R.; Hirayama, M. Discharge Performance of All-Solid-State Battery Using a Lithium Superionic Conductor $Li_{10}GeP_2S_{12}$. *Electrochemistry* **2012**, *80*, 749−751.

(3) Li, C.; Zhang, H.; Otaegui, L.; Singh, G.; Armand, M.; Rodriguez-Martinez, L. M. Estimation of Energy Density of Li-S Batteries with Liquid and Solid Electrolytes. *J. Power Sources* **2016**, *326*, 1−5.

(4) Janek, J.; Zeier, W. G. A Solid Future for Battery Development. *Nat. Energy* **2016**, *1*, 16141.

(5) Kato, Y.; Hori, S.; Saito, T.; Suzuki, K.; Hirayama, M.; Mitsui, A.; Yonemura, M.; Iba, H.; Kanno, R. High-Power All-Solid-State Batteries Using Sulfide Superionic Conductors. *Nat. Energy* **2016**, *1*, 1−7.

(6) Manthiram, A.; Yu, X.; Wang, S. Lithium Battery Chemistries Enabled by Solid-State Electrolytes. *Nat. Rev. Mater.* **2017**, *2*, 1−16.

(7) Xu, R. C.; Wang, X. L.; Zhang, S. Z.; Xia, Y.; Xia, X. H.; Wu, J. B.; Tu, J. P. Rational Coating of $Li_7P_3S_{11}$ Solid Electrolyte on $MoS_2$ Electrode for All-Solid-State Lithium Ion Batteries. *J. Power Sources* **2018**, *374*, 107−112.

(8) Kamaya, N.; Homma, K.; Yamakawa, Y.; Hirayama, M.; Kanno, R.; Yonemura, M.; Kamiyama, T.; Kato, Y.; Hama, S.; Kawamoto, K.; Mitsui, A. A Lithium Superionic Conductor. *Nat. Mater.* **2011**, *10*, 682−686.

(9) Bron, P.; Johansson, S.; Zick, K.; Schmedt auf Der Günne, J. S. A.; Dehnen, S.; Roling, B. $Li_{10}SnP_2S_{12}$: An Affordable Lithium Superionic Conductor. *J. Am. Chem. Soc.* **2013**, *135*, 15694−15697.

(10) Kato, A.; Yamamoto, M.; Sakuda, A.; Hayashi, A.; Tatsumisago, M. Mechanical Properties of $Li_2S$-$P_2S_5$ Glasses with Lithium Halides and Application in All-Solid-State Batteries. *ACS Appl. Energy Mater.* **2018**, *1*, 1002−1007.

(11) Seino, Y.; Ota, T.; Takada, K.; Hayashi, A.; Tatsumisago, M. A Sulphide Lithium Super Ion Conductor is Superior to Liquid Ion Conductors for Use in Rechargeable Batteries. *Energy Environ. Sci.* **2014**, *7*, 627−631.

(12) Ong, S. P.; Mo, Y.; Richards, W. D.; Miara, L.; Lee, H. S.; Ceder, G. Phase Stability, Electrochemical Stability and Ionic Conductivity of the $Li_{10\pm1}MP_2X_{12}$ (M = Ge, Si, Sn, Al or P, and X = O, S or Se) Family of Superionic Conductors. *Energy Environ. Sci.* **2013**, *6*, 148−156.

(13) Jung, W. D.; Kim, J.-S.; Choi, S.; Kim, S.; Jeon, M.; Jung, H.-G.; Chung, K. Y.; Lee, J.-H.; Kim, B.-K.; Lee, J.-H.; Kim, H. Superionic Halogen-Rich Li-Argyrodites Using In Situ Nanocrystal Nucleation and Rapid Crystal Growth. *Nano Lett.* **2020**, *20*, 2303−2309.

(14) Muramatsu, H.; Hayashi, A.; Ohtomo, T.; Hama, S.; Tatsumisago, M. Structural Change of $Li_2S$-$P_2S_5$ Sulfide Solid Electrolytes in the Atmosphere. *Solid State Ionics* **2011**, *182*, 116−119.

(15) Sahu, G.; Lin, Z.; Li, J.; Liu, Z.; Dudney, N.; Liang, C. Air-Stable, High-Conduction Solid Electrolytes of Arsenic-Substituted $Li_4SnS_4$. *Energy Environ. Sci.* **2014**, *7*, 1053−1058.

(16) Kaib, T.; Haddadpour, S.; Kapitein, M.; Bron, P.; Schröder, C.; Eckert, H.; Roling, B.; Dehnen, S. New Lithium Chalcogenidotetrelates, LiChT: Synthesis and Characterization of the $Li^+$-Conducting Tetralithium *ortho*-Sulfidostannate $Li_4SnS_4$. *Chem. Mater.* **2012**, *24*, 2211−2219.

(17) Zhang, Z.; Zhang, J.; Sun, Y.; Jia, H.; Peng, L.; Zhang, Y.; Xie, J. $Li_{4-x}Sb_xSn_{1-x}S_4$ Solid Solutions for Air-Stable Solid Electrolytes. *J. Energy Chem.* **2020**, *41*, 171−176.

(18) Ohtomo, T.; Mizuno, F.; Hayashi, A.; Tadanaga, K.; Tatsumisago, M. Electrical and Electrochemical Properties of $Li_2S$-$P_2S_5$-$P_2O_5$ Glass-Ceramic Electrolytes. *J. Power Sources* **2005**, *146*, 715−718.

(19) Ohtomo, T.; Hayashi, A.; Tatsumisago, M.; Kawamoto, K. Characteristics of the $Li_2O$-$Li_2S$-$P_2S_5$ Glasses Synthesized by the Two-Step Mechanical Milling. *J. Non-Cryst. Solids* **2013**, *364*, 57−61.

(20) Hayashi, A.; Muramatsu, H.; Ohtomo, T.; Hama, S.; Tatsumisago, M. Improvement of Chemical Stability of $Li_3PS_4$ Glass Electrolytes by Adding $M_xO_y$ (M = Fe, Zn, and Bi) Nanoparticles. *J. Mater. Chem. A* **2013**, *1*, 6320−6326.

(21) Hayashi, A.; Muramatsu, H.; Ohtomo, T.; Hama, S.; Tatsumisago, M. Improved Chemical Stability and Cyclability in $Li_2S$-$P_2S_5$-$P_2O_5$-ZnO Composite Electrolytes for All-Solid-State Rechargeable Lithium Batteries. *J. Alloys Compd.* **2014**, *591*, 247−250.
(22) Xie, D.; Chen, S.; Zhang, Z.; Ren, J.; Yao, L.; Wu, L.; Yao, X.; Xu, X. High Ion Conductive $Sb_2O_5$-Doped B-$Li_3PS_4$ with Excellent Stability against Li for All-Solid-State Lithium Batteries. *J. Power Sources* **2018**, *389*, 140−147.
(23) Adeli, P.; Bazak, J. D.; Park, K. H.; Kochetkov, I.; Huq, A.; Goward, G. R.; Nazar, L. F. Boosting Solid-State Diffusivity and Conductivity in Lithium Superionic Argyrodites by Halide Substitution. *Angew. Chem., Int. Ed.* **2019**, *58*, 8681−8686.
(24) Yu, C.; Ganapathy, S.; Hageman, J.; van Eijck, L.; van Eck, E. R. H.; Zhang, L.; Schwietert, T.; Basak, S.; Kelder, E. M.; Wagemaker, M. Facile Synthesis toward the Optimal Structure-Conductivity Characteristics of the Argyrodite $Li_6PS_5Cl$ Solid-State Electrolyte. *ACS Appl. Mater. Interfaces* **2018**, *10*, 33296−33306.
(25) Boulineau, S.; Courty, M.; Tarascon, J.-M.; Viallet, V. Mechanochemical synthesis of Li-argyrodite $Li_6PS_5X$ (X=Cl, Br, I) as sulfur-based solid electrolytes for all solid state batteries application. *Solid State Ionics* **2012**, *221*, 1−5.
(26) Han, F.; Zhu, Y.; He, X.; Mo, Y.; Wang, C. Electrochemical Stability of $Li_{10}GeP_2S_{12}$ and $Li_7La_3Zr_2O_{12}$ Solid Electrolytes. *Adv. Energy Mater.* **2016**, *6*, 1501590.
(27) Wang, Z.; Shao, G. Theoretical Design of Solid Electrolytes with Superb Ionic Conductivity: Alloying Effect on $Li^+$ Transportation in Cubic $Li_6PA_5X$ Chalcogenides. *J. Mater. Chem. A* **2017**, *5*, 21846−21857.
(28) Lim, H.-D.; Lim, H.-K.; Xing, X.; Lee, B.-S.; Liu, H.; Coaty, C.; Kim, H.; Liu, P. Solid Electrolyte Layers by Solution Deposition. *Adv. Mater. Interfaces* **2018**, *5*, 1701328.
(29) Yubuchi, S.; Uematsu, M.; Deguchi, M.; Hayashi, A.; Tatsumisago, M. Lithium-Ion-Conducting Argyrodite-Type $Li_6PS_5X$ (X = Cl, Br, I) Solid Electrolytes Prepared by a Liquid-Phase Technique Using Ethanol as a Solvent. *ACS Appl. Energy Mater.* **2018**, *1*, 3622−3629.
(30) Wu, X.; El Kazzi, M.; Villevieille, C. Surface and Morphological Investigation of the Electrode/Electrolyte Properties in an All-Solid-State Battery Using a $Li_2S$-$P_2S_5$ Solid Electrolyte. *J. Electroceram.* **2017**, *38*, 207−214.
(31) Oh, D. Y.; Ha, A. R.; Lee, J. E.; Jung, S. H.; Jeong, G.; Cho, W.; Kim, K. S.; Jung, Y. S. Wet-Chemical Tuning of $Li_{3-x}PS_4$ ($0 \leq x \leq 0.3$) Enabled by Dual Solvents for All-Solid-State Lithium-Ion Batteries. *ChemSusChem* **2019**, *13*, 1−151.
(32) Takada, K.; Osada, M.; Ohta, N.; Inada, T.; Kajiyama, A.; Sasaki, H.; Kondo, S.; Watanabe, M.; Sasaki, T. Lithium Ion Condutive Oxysulfide, $Li_3PO_4$−$Li_3PS_4$. *Solid State Ionics* **2005**, *176*, 2355−2359.
(33) Riphaus, N.; Strobl, P.; Stiaszny, B.; Zinkevich, T.; Yavuz, M.; Schnell, J.; Indris, S.; Gasteiger, H. A.; Sedlmaier, S. J. Slurry-Based Processing of Solid Electrolytes: A Comparative Binder Study. *J. Electrochem. Soc.* **2018**, *165*, A3993−A3999.
(34) Chen, S.; Wang, J.; Zhang, Z.; Wu, L.; Yao, L.; Wei, Z.; Deng, Y.; Xie, D.; Yao, X.; Xu, X. In-situ Preparation of Poly(Ethylene Oxide)/$Li_3PS_4$ Hybrid Polymer Electrolyte With Good Nanofiller Distribution for Rechargeable Solid-State Lithium Batteries. *J. Power Sources* **2018**, *387*, 72−80.
(35) Inada, T.; Takada, K.; Kajiyama, A.; Kouguchi, M.; Sasaki, H.; Kondo, S.; Watanabe, M.; Murayama, M.; Kanno, R. Fabrications and Properties of Composite Solid-State Electrolytes. *Solid State Ionics* **2003**, *158*, 275−280.
(36) Lee, K.; Lee, J.; Choi, S.; Char, K.; Choi, J. W. Thiol-Ene Click Reaction for Fine Polarity Tuning of Polymeric Binders in Solution-Processed All-Solid-State Batteries. *ACS Energy Lett.* **2019**, *4*, 94−101.
(37) Lee, K.; Kim, S.; Park, J.; Park, S. H.; Coskun, A.; Jung, D. S.; Cho, W.; Choi, J. W. Selection of Binder and Solvent for Solution-Processed All-Solid-State Battery. *J. Electrochem. Soc.* **2017**, *164*, A2075−A2081.
(38) Kleiman, M.; Ryu, K. A.; Esser-Kahn, A. P. Determination of Factors Influencing the Wet Etching of Polydimethylsiloxane Using Tetra-n-butylammonium Fluoride. *Macromol. Chem. Phys.* **2016**, *217*, 284−291.
(39) Wang, K.; Wang, M. Hyperbranched Narrow-Bandgap DPP Homopolymers Syntthesized via Direct Arylation Polycondensation. *J. Polym. Sci., Part A: Polym. Chem.* **2017**, *55*, 1040−1047.
(40) Oh, D. Y.; Nam, Y. J.; Park, K. H.; Jung, S. H.; Kim, K. T.; Ha, A. R.; Jung, Y. S. Slurry-Fabricable $Li^+$-Conductive Polymeric Binders for Practical All-Solid-State Lithium-Ion Batteries Enabled by Solvate Ionic Liquids. *Adv. Energy Mater.* **2019**, *9*, 1−10.
(41) Oh, D. Y.; Nam, Y. J.; Park, K. H.; Jung, S. H.; Cho, S.-J.; Kim, Y. K.; Lee, Y.-G.; Lee, S.-Y.; Jung, Y. S. Excellent Compatibility of Solvate Ionic Liquids with Sulfide Solid Electrolytes: Toward Favorable Ionic Contacts in Bulk-Type All-Solid-State Lithium-Ion Batteries. *Adv. Energy Mater.* **2015**, *5*, 1−7.
(42) Yamamoto, M.; Terauchi, Y.; Sakuda, A.; Takahashi, M. Binder-Free Sheet-Type All-Solid-State Batteries with Enhanced Rate Capabilities and High Energy Densities. *Sci. Rep.* **2018**, *8*, 2−11.
(43) Byrne, F. P.; Forier, B.; Bossaert, G.; Hoebers, C.; Farmer, T. J.; Hunt, A. J. A Methodical Selection Process for the Development of Ketones and Esters as Bio-based Replacements for Traditional Hydrocarbon Solvents. *Green Chem.* **2018**, *20*, 4003−4011.
(44) Hencz, L.; Chen, H.; Ling, H. Y.; Wang, Y.; Lai, C.; Zhao, H.; Zhao, S. Housing Sulfur in Polymer Composite Frameworks for Li-S Batteries. *Nano-Micro Lett.* **2019**, *11*, 17.
(45) Zhang, J.; Zhong, H.; Zheng, C.; Xia, Y.; Liang, C.; Huang, H.; Gan, Y.; Tao, X.; Zhang, W. All-Solid-State Batteries with Slurry Coated $LiNi_{0.8}Co_{0.1}Mn_{0.1}O_2$ Composite Cathode and $Li_6PS_5Cl$ Electrolyte: Effect of Binder Content. *J. Power Sources* **2018**, *391*, 73−79.
(46) Rosero-Navarro, N. C.; Miura, A.; Tadanaga, K. Preparation of Lithium Ion Conductive $Li_6PS_5Cl$ Solid Electrolyte from Solution for the Fabrication of Composite Cathode of All-Solid-State Lithium Battery. *J. Sol-Gel Sci. Technol.* **2019**, *89*, 303−309.


https://dx.doi.org/10.1021/acsomega.0c03453
*ACS Omega* 2020, 5, 26015−26022